Electronic structure of $LaNiO_2$ and $CaCuO_2$ from a self-consistent vertex-corrected *GW* approach

Andrey L. Kutepov*

Condensed Matter Physics and Materials Science Department, Brookhaven National Laboratory, Upton, New York 11973, USA

(Received 8 May 2021; accepted 28 July 2021; published 6 August 2021)

The electronic structure of one of the nickelates ($LaNiO_2$) and one of the cuprates ($CaCuO_2$) is studied with three self-consistent *GW*-based methods: sc*GW*, sc(*GW*+vertex), and quasiparticle self-consistent *GW*. Low-energy features obtained in our study are in many respects similar to the features reported in previous density functional theory plus dynamical mean-field theory (DFT+DMFT) studies. Consistent with the DFT+DMFT conclusion, we find $LaNiO_2$ to be more correlated than $CaCuO_2$. However, correlation effects included in our study change the DFT Fermi surface near the Γ point differently from that reported in DMFT studies. Features that are a few electronvolts away from the Fermi level are broader in our calculations than in the DFT+DMFT, which reflects the differences between the DFT and the *GW* methods. Our results are in qualitative agreement with previous *G*0*W*0 results, but the self-consistency results in quantitative differences. Generally, correlation effects are found to be sufficiently weak in both materials, which allows one to use totally *ab initio* diagrammatic approaches such as sc(*GW*+vertex) and to avoid the methods with adjustable parameters (DFT+U or DFT+DMFT). However, the possibility of some strong correlations at low energy that cannot be captured by perturbative methods cannot be completely excluded. For instance, differences in the Fermi surface should be resolved, thus experimental studies are necessary.

DOI: 10.1103/PhysRevB.104.085109

I. INTRODUCTION

The recent experimental discovery of superconductivity in hole-doped $NdNiO_2$ generated renewed interest in nickelates. In particular, the similarities and differences between nickelates and cuprates were studied intensely during the past couple of years. Such study has obvious importance as it can potentially reveal the features in the electronic structure that are responsible for the differences in superconducting properties. Very often, the study was concerned with $LaNiO_2$ and $CaCuO_2$ as simple representatives of both families of materials (nickelates and cuprates, respectively). On the theoretical (calculational) side, the majority of the work was based on the density functional theory [1–7] (DFT), or on DFT plus dynamical mean-field theory (DFT+DMFT) [4,5,8,9] calculations. Only one calculation based on the *GW* terminology applying its non-self-consistent version (*G*0*W*0) was published recently [10]. From a methodological point of view, it is important to mention also the application of the *GW*+DMFT approach to the related compound $NdNiO_2$ [11]. Before proceeding with the present work, let us briefly detail the results from other works that are the most relevant to the present study.

At the DFT level, the principal difference between the two materials consists of the increased energy separation [2] of the Ni $3d_{x^2-y^2}$ orbitals from the O $2p$ orbitals in $LaNiO_2$ as compared to the corresponding separation of the Cu $3d_{x^2-y^2}$ and the O $2p$ orbitals in $CaCuO_2$. Also, the $5d$ orbitals of La cross the Fermi level in $LaNiO_2$ and, therefore, are coupled with the Ni $3d_{x^2-y^2}$ orbitals. At the DFT+DMFT level, Wang *et al.* [5] studied two nickelates, $SrNiO_2$ and $LaNiO_2$. In their study, all Ni $3d$ orbitals were considered as correlated with the Hubbard U parameter 5 eV. A visual comparison of the electronic structure of $LaNiO_2$ obtained in [5] at the DFT and the DFT+DMFT levels (Fig. 2 in their work) does not reveal any qualitative differences on the scale of a few electronvolts. One can see the renormalization of bands only in the immediate vicinity of the Fermi level. Karp *et al.* [4] used the DFT+DMFT to compare $NdNiO_2$ and $CaCuO_2$. Instead of considering all Ni(Cu) $3d$ states as correlated, the authors of Ref. [4] performed two types of DFT+DMFT calculations: one with only Ni(Cu) $3d_{x^2-y^2}$ as a correlated orbital, and the second with Ni(Cu) $3d_{x^2-y^2}$ and $3d_{3z^2-r^2}$ as correlated. The Hubbard parameter U was, correspondingly, increased from 3.1 eV in the first type of calculation to 7 eV in the second one. The important conclusion from this work is that nickelates are more correlated than cuprates (see Fig. 2 in Ref. [4]). Also, the authors place nickelates in the same charge-transfer category of materials as the cuprates despite the larger separation between the $d_{x^2-y^2}$ and the O $2p$ states in the nickelates. One more important difference is that the rare-earth d states appear in both the addition and removal spectra in nickelates, which is a sign of their hybridization with Ni $3d$ states.

The above-mentioned DFT and DFT+DMFT works provide insightful information on the materials. One can point out, however, that there are certain issues, particularly with the DFT+DMFT, which can affect the robustness of the conclusions. First, the DFT+DMFT results depend on the choice of the U parameter. In this respect, the choice of U in Refs. [4] and [5] seems to be inconsistent. In the first work, the U parameter was 3.1 eV for one correlated orbital and 7 eV for

*akutepov@bnl.gov

two correlated orbitals. The more orbitals that we consider as correlated, the larger U should be because the screening by the rest of the (uncorrelated) orbitals is reduced. However, in Ref. [5], where all five Ni $3d$ orbitals were correlated, the U value was only 5 eV. Second, because of the apparent importance of the energy separation between the Ni(Cu) $3d$ and the O $2p$ levels and of the degree of the hybridization between Ni $3d$ and La $5d$, the neglect by the intersite (nonlocal) components of self-energy in both the DFT and the DFT+DMFT studies seems to be highly questionable when considering the relative positioning of the Ni(Cu) $3d$ and O $2p$ states, and Ni $3d$ and La $5d$. Third, low-energy physics (in the immediate vicinity of the Fermi level), which is the principal goal of the DFT+DMFT studies, can most likely also be impacted by the effects that are not included in the DFT+DMFT: electron-phonon interaction, the same nonlocal self-energy effects, and the frequency dependence of the effective interaction. Therefore, the conclusions might change when all important contributions are properly taken into account.

Thus, it seems to be important and interesting to also apply other methods, which include correlation effects and which are free of at least some of the mentioned issues of the DFT+DMFT. In this respect, the work by Olevano *et al.* [10] represents an important step. In their work, the non-self-consistent *GW* approximation ($G0W0$) was used to study the electronic structure of $LaNiO_2$. $G0W0$ represents only the first term in the expansion of self-energy, but it includes all nonlocal physics on the same footing as the local one. Plus, it has no adjustable parameters and it considers the full frequency-dependent effective interaction. The authors of Ref. [10] have shown that the La $4f$ states undergo a 2 eV upward shift with respect to their DFT position, whereas the O $2p$ states are pulled down by 1.5 eV. Thus, they stress the importance of the nonlocal physics in this compound. As a drawback of the $G0W0$ approximation, one can consider its obvious dependence on the starting point (because of the lack of self-consistency). $G0W0$ relies on the assumption that *GW* wave functions are similar to the DFT wave functions (if the DFT is used as a starting point). This assumption works well in simple semiconductors (such as Si or LiF), but it can be seriously questioned in more complicated materials. For instance, the $G0W0$ (with the DFT as a starting point) applied to the monoclinic M1 phase of VO_2 results in a metal (similar to the DFT), whereas it is an insulator in experiments [12]. Only the self-consistent quasiparticle *GW* calculation provides the correct insulating state [13]. With this consideration, it is clear that the self-consistent calculations based on the *GW* calculations can provide essential new information on the differences in the electronic structure of $LaNiO_2$ and $CaCuO_2$.

The principal goal of this work is, therefore, to apply the self-consistent *GW* method to the representatives of nickelates and cuprates. We also apply the self-consistent GW+vertex approach to determine the strength of the correlation effects beyond the *GW* approximation. Plus, we apply the self-consistent quasiparticle *GW* approximation (QSGW) as it stresses the importance of the Ward identity (WI) in the limit of low frequency and low momenta, but it neglects the dynamical effects (frequency dependence) in self-energy. The scGW, on the other hand, treats the high-frequency part of the self-energy on the same footing as the low-frequency part but neglects the WI altogether.

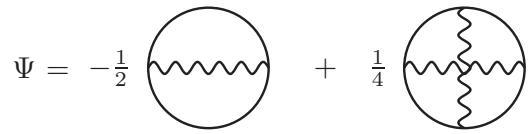

FIG. 1. Diagrammatic representation of the Ψ-functional, which includes the simplest nontrivial vertex.

The paper begins with a brief discussion on the distinctive features of the methods used in this work and setup parameters for the calculations (the first section). The second section provides the results obtained and a discussion. The conclusions are given in the final section. Finally, three Appendixes provide supporting information for the main text.

II. METHODS AND CALCULATION SETUPS

All calculations in this work were performed using the code FLAPWMBPT [14]. For the DFT calculations, we used the local density approximation (LDA) as parametrized by Perdew and Wang [15]. Recently, a number of improvements in the quality of the basis set in the FLAPWMBPT code have been implemented [16], which enabled, for instance, a more accurate evaluation of the atomic forces [17]. Our scGW and sc(GW+vertex) calculations are based on Hedin's theory [18]. They can also be defined using the Ψ-functional formalism of Almbladh *et al.* [19]. As is shown in Ref. [19], the Ψ-functional can be constructed starting from the Luttinger-Ward Φ-functional [20] and using screened Coulomb interaction W instead of bare Coulomb interaction V as an independent variable (in addition to Green's function G). It is defined by the following expression:

$$\Psi[G,W] = \Phi[G,V] - \tfrac{1}{2}\mathrm{Tr}[PW - \ln(1+PW)], \quad (1)$$

where P is the irreducible polarizability. In materials science, the Ψ-functional is more convenient than the Φ-functional of Luttinger and Ward. The first reason is connected to the infinite range of the bare Coulomb interaction, which makes the screened interaction W a much more suitable quantity than the bare interaction V. The second reason is the simplicity of the Ψ-functional. For instance, at the level of the *GW* approximation, the Φ-functional is represented by an infinite sequence of ring diagrams, whereas the Ψ-functional is represented by just one diagram (the first diagram in Fig. 1). In this work, the simplest approximation for the Ψ-functional, which includes vertex corrections, has been adapted (Fig. 1). As was already mentioned, the first diagram in Fig. 1 corresponds to the *GW* approximation, whereas the second one represents the first-order vertex correction.

Diagrammatic representations for irreducible polarizability (Fig. 2) and for self-energy (Fig. 3) follow from the chosen approximation for the Ψ-functional. The set of diagrams for polarizability and self-energy shown in Figs. 2 and 3 corresponds to scheme B introduced earlier in Ref. [21]. To make the notations more self-explanatory, here we introduce another abbreviation. Following the convention for the *GW* approach which corresponds to the lines of the *GW*

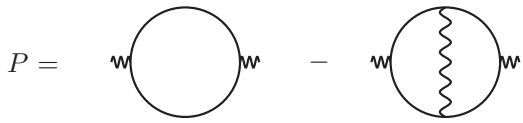

FIG. 2. Diagrammatic representation of irreducible polarizability in the simplest vertex-corrected scheme.

diagram (the first diagram in Fig. 3), we will use the term sc($GW + G3W2$) [instead of sc(GW+vertex) or "scheme B"], which corresponds to all diagrams in Fig. 3. A specific diagrammatic representation of polarizability defines the approximation for screening. Thus, from Fig. 2 we can state that in sc($GW + G3W2$) the screening is defined by the one-loop diagram [random phase approximation (RPA)] plus the first-order electron-hole interaction diagram. scGW includes only the RPA part. The technical details of the GW part were described in Refs. [22,23]. The numerical algorithm for the evaluation of first-order polarizability was the same in this study as that described in detail in Ref. [21]. For the evaluation of second-order self-energy, however, a more efficient algorithm (as compared to the one described in [21]) is used. The brief account of the details of this new algorithm can be found in the Appendix A. The diagrammatic (GW and $G3W2$) parts of the FLAPWMBPT code take full advantage of the fact that certain diagrams can be evaluated more efficiently in reciprocal (and frequency) space, whereas other diagrams are easier to evaluate in real (and time) space. As a result, the GW part of the code scales as $N_k N_\omega N_b^3$, where N_k is the number of **k**-points in the Brillouin zone, N_ω is the number of Matsubara frequencies, and N_b stands for the size of the basis set. The vertex part of the code scales as $N_k^2 N_\omega^2 N_b^4$. For comparison, if one uses a naive (all in reciprocal space and frequency) implementation, then the GW part scales as $N_k^2 N_\omega^2 N_b^4$ (i.e., exactly as the vertex part when the implementation is efficient), and the vertex part scales as $N_k^3 N_\omega^3 N_b^5$. In addition to the efficiency of the implementation, we have to mention two more factors that make use of the diagrams beyond GW feasible. First, the higher-order diagrams converge much faster than the GW diagram with respect to the basis-set size and to the number of **k**-points [21,24]. Second, the higher-order diagrams are very well suited for massive parallelization.

scGW has a certain advantage as compared to the non-self-consistent (one shot) $G0W0$ approach: there is no dependence on the starting point in scGW. Also, being based on the functional formalism, it provides (at least in principle) a direct way to evaluate the total energies [25–27]. However, from a purely theoretical point of view, scGW has certain issues that one can relate to the rather "nonsymmetric" dressing of the Green function during the self-consistency course: adding

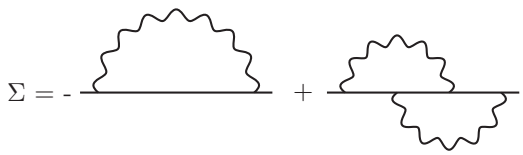

FIG. 3. Diagrammatic representation of self-energy in the simplest vertex-corrected scheme.

more and more self-consistency diagrams while retaining at each iteration only the lowest-order skeleton diagram for polarizability and for self-energy. This "nonsymmetric" dressing results in, for instance, an incorrect long-wave limit of polarizability. There are quite a few documented limitations of the approach, e.g., the bandwidth in electron gas [25] and in alkali metals [28] is too big (as compared to the correct result), there is an absence of satellites in electron gas [25], and there is an overestimation of the band gap in simple semiconductors [28,29]. To "defend" scGW a bit, one can observe that the above-mentioned limitations pertain mostly to the materials in which nonlocal physics is prevalent (electron gas, alkali metals, sp semiconductors). There is only a limited number of scGW applications to the realistic materials where local effects are the most important or, at least, contribute considerably to observable properties. Existing applications, however, are not as conclusive as in the case of simple materials. Just to name a few, scGW overestimates the magnetic moment in iron [27] and the band gap in NiO [30]. Also, in $SrVO_3$, there is an indication of worsening of the calculated spectra when going from $G0W0$ to scGW [31]. However, scGW in Ref. [31] was implemented for a rather small basis set (only $t2g$ orbitals), which means that the conclusion, though plausible, is not very convincing. On the other hand, scGW describes perfectly well the experimental photoemission spectrum of metal americium [22], whereas $G0W0$ fails completely. Also, applications of scGW are rather popular in atomic and molecular physics [32–34], which supports the idea that in the world of "finite systems," scGW has certain merits.

sc($GW + G3W2$) adds skeleton diagrams of the next order (as compared to scGW) to both polarizability and self-energy. Therefore, the problems occurring because of the above-described "nonsymmetric" dressing of the Green's function should be less dramatic. From this point of view, one can expect sc($GW + G3W2$) to be more accurate than scGW. Indeed, there is a noticeable improvement in the calculated bandwidth of the electron gas [35] and alkali metals [21]. Improvements in the calculated band gap of sp semiconductors are especially remarkable [24]. In the case of simple semiconductors, sc($GW + G3W2$) not only outperforms scGW and QSGW considerably (see the Introduction), but it is also better than $G0W0$ in most cases. For more complicated materials, one can point out a recent calculation of the band gap in NiO [30] where sc($GW + G3W2$) resulted in an almost perfect reproduction of the experimental gap, whereas scGW overestimated it by about 25%. Also, the improvement in the calculated band gap of the van der Waals ferromagnet CrI_3 is considerable [36]. Of course, one cannot expect that sc($GW + G3W2$) will be considerably better than scGW in the case of really strongly correlated materials, i.e., where nonperturbative treatment is necessary.

We also use the quasiparticle self-consistent GW (QSGW) approach. Similar to the scGW and the sc($GW + G3W2$) approaches, it is based on the finite-temperature (Matsubara) formalism, and in this respect it is different from the well-known QSGW implementation by Kotani *et al.* [37]. The quasiparticle approximation includes linearization of self-energy near zero frequency (for details, see Refs. [22,23]), and therefore the method is only reliable not very far from the Fermi level—usually within a few electronvolts. The

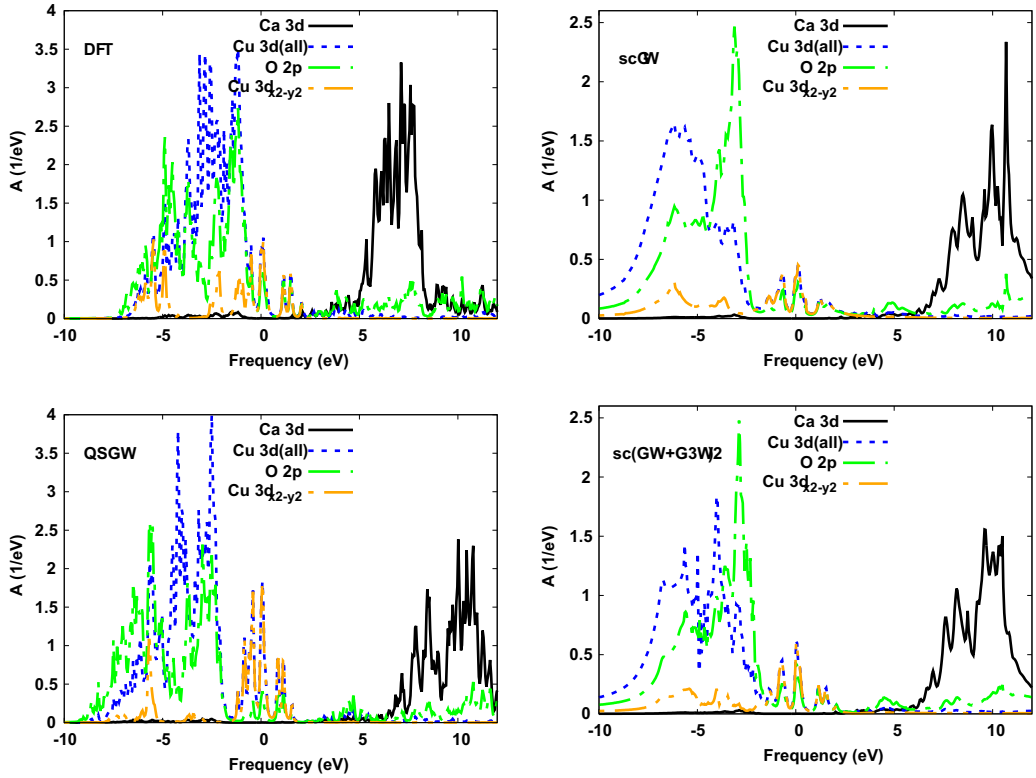

FIG. 4. Partial (atom and orbital resolved) spectral functions of $CaCuO_2$.

approach adopted by Kotani *et al.* in Ref. [37] uses a specially designed procedure of averaging of nondiagonal elements of self-energy for each quasiparticle state instead of the linearization near the chemical potential. This fact, presumably, should make the approach of Kotani *et al.* more accurate in a broad energy range than QSGW used in this study. However, for energies not far from the chemical potential (the range of interest in this work), two types of QSGW are quite similar. The differences, in fact, are mostly related to the differences in basis sets and in the degree of convergence [24]. In both variants of QSGW, the effective self-energy is static (frequency-independent; see Appendix B) and the method is not diagrammatic. Special (or rather manual) construction of the effective self-energy breaks its relation to the Ψ-functional. However, as was explained by Kotani *et al.* [37], QSGW satisfies the zero-frequency and long-wave limit of the Ward identity because of the so called Z-factor cancellation. As a result, it is often quite accurate, especially in simple metals and semiconductors, where the above-mentioned limit is important. Band gaps, calculated with the QSGW, for instance, are usually more accurate than the ones calculated with the scGW [24,29,38]. In more complicated solids (especially where d or f electrons play an important role), the QSGW approach is not necessarily better than the scGW: the frequency dependence of self-energy could be more important than the zero-frequency+momentum limit of the WI. A good example is the metal americium, where both the DFT and the QSGW fail to describe the experimentally determined [39] position of the occupied $5f_{5/2}$ states, whereas scGW describes them very well [22]. For simple (sp) semiconductors with a large band gap (C, MgO, LiF, NaCl), scGW outperforms QSGW [24,29] (not considerably, though). Also, as it seems [36], scGW is slightly more accurate than QSGW in the case of CrI_3. Additional insight into the differences between the approximate methods of this work is provided in Appendix C. Considering their differences, the three approaches [scGW, sc($GW + G3W2$), and QSGW] represent a good set of methods to study new materials.

Our algorithm for the analytical continuation of self-energy, which was needed, for instance, to plot Figs. 4 and 5, is based on Ref. [40] and it is described in the Appendix of Ref. [41]. The band plotting associated with the scGW/sc($GW + G3W2$) approach (see Fig. 7) needs some additional clarification. Strictly speaking, one-electron features (band dispersions) in these two approaches should be obtained as the peak positions of the **k**-resolved spectral functions. An evaluation of spectral functions includes the analytical continuation of the correlation part of self-energy from the imaginary to the real frequency axis. However, as was demonstrated in Refs. [22,41], the peak positions of the spectral function near the chemical potential can often be accurately reproduced by a simplified procedure. This procedure involves the linearization of the frequency dependence of self-energy near the chemical potential, and consequently it results in the effective one-electron energies (see details in the Appendix of Ref. [41]). The one-electron energies, thus obtained, can obviously be used for band plotting purposes.

Let us now specify the setup parameters used in the calculations. To make the presentation more compact, principal structural parameters for the studied solids have been collected in Table I, and the most important setup parameters have been collected in Table II. All calculations have been

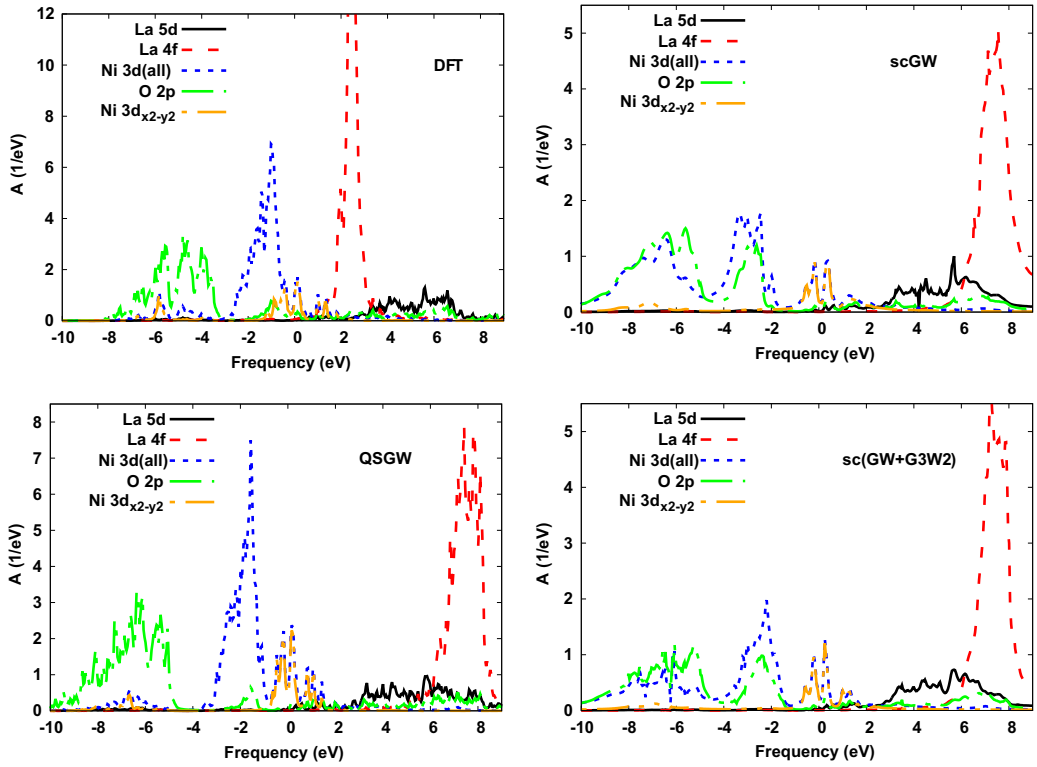

FIG. 5. Partial (atom and orbital resolved) spectral functions of $LaNiO_2$.

performed for the electronic temperature 600 K. As the long-range magnetic order has not yet been found in $LaNiO_2$, all calculations were nonmagnetic for simplicity. The DFT, scGW, QSGW, and GW parts in the sc($GW + G3W2$) calculations were performed with the $6 \times 6 \times 6$ mesh of **k**-points in the Brillouin zone. A total of 300 band states were used to expand the Green's function and the self-energy. The convergence provided by the above parameters was checked by doing calculations with a $4 \times 4 \times 4$ mesh of **k**-points and with a smaller number of bands for the GW part. From the analysis we conclude that further increase in the number of **k**-points and bands should not change the effective band energies near the Fermi level (Fig. 7) by more than 5%, which is sufficient for the comparison of the methods. The diagrams beyond the GW approximation were evaluated using a $3 \times 3 \times 3$ mesh of **k**-points in the Brillouin zone and with about 26 bands (closest to the Fermi level). With the above-mentioned faster convergence of the higher-order diagrams with respect to these parameters, this choice represented a reasonable compromise between the accuracy and the computational cost. Similar to the GW part, the convergence was checked by doing calculations with a smaller number of **k**-points ($2 \times 2 \times 2$) and of bands (10–22 instead of the final 26). We estimate the error of the vertex part [i.e., the difference between sc($GW + G3W2$) and scGW results] to be about or less than 10–15 %. Again, from Fig. 7 one can see that the above difference is rather small, so that if it changes by 10–15 % the conclusions will be the same.

III. RESULTS

Partial (atom and orbital resolved) spectral functions are presented in Fig. 4 ($CaCuO_2$) and in Fig. 5 ($LaNiO_2$). First, let us point out that there are a few important differences in the electronic structure of these two materials at the DFT level. First, the La $4f$ levels in $LaNiO_2$ dominate in the energy range immediately above the Fermi level. The La $5d$ states are spread in energy and are above the $4f$ states by 2–5 eV. The absence of the f-states in $CaCuO_2$ makes the presence of the Ca $3d$ states more prominent among the unoccupied bands. The character of the levels at the Fermi level also represents an important qualitative difference. In $CaCuO_2$, they are almost equally represented by the Cu $3d_{x^2-y^2}$ and the O $2p$ states. In $LaNiO_2$, however, the $3d_{x^2-y^2}$ states of Ni dominate. The states below the Fermi level also look different. In $CaCuO_2$, the Cu $3d$ states are mixed with the O $2p$ states and together they occupy the same energy range from -7 eV to almost the Fermi level. In $LaNiO_2$, the Ni $3d$ states are well separated from the O $2p$ states and they occupy the energy range from

TABLE I. Structural parameters of the solids studied in this work. Lattice parameters are in angstroms, MT radii are in atomic units (1 Bohr radius), and atomic positions are given relative to the three primitive translation vectors.

Solid	Space group	a	c	Atomic positions	R_{MT}
$CaCuO_2$	123	3.86	3.20	Ca: 0;0;0	2.032
				Cu: 1/2;1/2;1/2	2.032
				O: 1/2;0;1/2	1.563
$LaNiO_2$	123	3.966	3.376	La: 0;0;0	2.087
				Ni: 1/2;1/2;1/2	2.087
				O: 1/2;0;1/2	1.606

TABLE II. Principal setup parameters of the studied solids are given. The following abbreviations are introduced: Ψ is for wave functions, ρ is for the electronic density, V is for Kohn-Sham potential, and PB is for the product basis.

Solid	Core states	Semicore	$L_{\max}$ $\Psi/\rho, V$	$L_{\max}$ PB	$RK_{\max}$
$CaCuO_2$	Ca: [Ne]	$3s, 3p$	6/6	6	8.0
	Cu: [Ne]	$3s, 3p$	6/6	6	
	O: [He]	$2s$	5/5	5	
$LaNiO_2$	La: [Ar]$3d$	$4s, 4p, 4d, 5s, 5p$	6/6	6	8.0
	Ni: [Ne]	$3s, 3p$	6/6	6	
	O: [He]	$2s$	5/5	5	

-3 eV to the Fermi level, whereas the O $2p$ states occupy the energy range from -8 to -3.5 eV.

Let us now discuss the changes in the electronic structure (as compared to the DFT) when we apply the fully self-consistent GW approach. In $CaCuO_2$, there are no qualitative changes. For instance, states at the Fermi level are still equally represented by the Cu $3d_{x^2-y^2}$ and the O $2p$ states. Also, part of the spectral weight associated with the Cu $3d_{x^2-y^2}$ states still resides in the occupied valence bands. The occupied Cu $3d$ states are strongly mixed with the O $2p$ states as in the DFT case. However, these joint occupied states are shifted down by about 2 eV as compared to the DFT case. The unoccupied Ca $3d$ states are shifted up by about 2 eV. In $LaNiO_2$, the states immediately at the Fermi level are still almost completely represented by the Ni $3d_{x^2-y^2}$ orbitals, as in the DFT calculations. However, the rest of the electronic structure is qualitatively different from the DFT case. First, the La $4f$ states are pushed up by about 5 eV in the scGW calculations as compared to the DFT. Now they are above the La $5d$ bands, and supposedly they are not very important for the low-energy physics. But an even more noticeable change is related to the fact that the occupied Ni $3d$ and the O $2p$ states, which were very well separated in the DFT calculations, are now strongly mixed and reside in the same energy range from approximately -10 to -2 eV relative to the Fermi level. As one can notice, this was achieved by a considerable down push of the occupied Ni $3d$ states and by a slight (about 1 eV) push of the O $2p$ states up in energy.

The self-consistent vertex-corrected GW calculations do not change the scGW result very much. One can notice, however, that in both materials the occupied Ni(Cu) $3d$ and O $2p$ states were pushed up in energy by about 0.5 eV (compared to the scGW result). A very slight downward push of the Ca $3d$ (La $5d$) can also be noticed.

The QSGW calculations for $CaCuO_2$ result in an electronic structure very similar to that obtained with the scGW/sc$(GW + G3W2)$ approach, which can be verified by comparison of the positions of all principal peaks in Fig. 4. The situation with $LaNiO_2$ is, however, quite different. Contrary to the scGW and the sc$(GW + G3W2)$ calculations, the QSGW shows only quantitative (but not qualitative) changes in the electronic structure (as compared to the DFT). The only obvious similarity with the scGW results is the upward shift of the La $4f$ states. The oxygen $2p$ and the occupied Ni $3d$ states are pushed downward by -2 and -1 eV, respectively, but there is no mixing among them as in the scGW or the sc$(GW + G3W2)$ case. Obviously, in the case of $LaNiO_2$ the differences in methods—the QSGW on the one hand and the scGW/sc$(GW + G3W2)$ on the other hand—are a lot more prominent than in the case of $CaCuO_2$.

It is interesting to compare the tendencies in the electronic structure of $LaNiO_2$ (when we go from the LDA to more complicated methods) with the tendencies discovered in Ref. [10]. The principal finding of Ref. [10] is that La $4f$ states are pushed up by about 2 eV in the $G0W0$ calculation (as compared to the DFT), O $2p$ states are pushed down by about -1.5 eV, and the energy levels near the Fermi level do not change noticeably. The energy levels near the Fermi level are represented by Ni $3d_{x^2-y^2}$ orbitals in all our calculations. In this respect, we agree with earlier $G0W0$ calculations. Furthermore, all our post-DFT approaches push La $4f$ states up by about 5 eV, which is larger than 2 eV in the $G0W0$ case and can naturally be explained by self-consistency effects. The change in the position of O $2p$ states is, however, different. Only our QSGW approach agrees with the $G0W0$ finding: a downward push by about -1.5 eV. As was already discussed above, the methods with dynamic self-energy [scGW and sc$(GW + G3W2)$] demonstrate a qualitatively different change: O $2p$ states split into two groups with the boundary between groups at about -4 eV, and they mix considerably with Ni $3d$ states. The difference in this tendency is, most likely, related to the incoherence effects in self-consistency diagrams, which are not included in the $G0W0$ or QSGW approaches.

To take a measure of the strength of the correlation effects, the renormalization factor Z has been evaluated. Results are shown in Fig. 6 for the Γ point of the Brillouin zone. As one can see, all approaches [scGW, sc$(GW + G3W2)$, and QSGW] result in quite similar and moderate correlation effects. A minimal value of Z is unmistakably obtained for one band near the Fermi level, which has Ni(Cu) $3d_{x^2-y^2}$ character. This holds for all points in the Brillouin zone in the case of $LaNiO_2$. For $CaCuO_2$, however, there is a noticeable admix of the O $2p$ character in some parts of the Brillouin zone (not shown in Fig. 6). In those points, the Z factor is slightly larger (up to 0.77–0.80). Generally, analysis of the Z factor confirms that the correlations are slightly stronger in the $LaNiO_2$ case. In this respect, our calculations are in line with all published works. Also, similar to the $G0W0$ calculations [10], we obtained very little variation of Z across the Brillouin zone for the Ni $3d_{x^2-y^2}$ band in the case of $LaNiO_2$. Its value is also very close to the value 0.70 ± 0.02 reported in the $G0W0$ calculations. There are, however, differences with the DFT+DMFT results. Most notable is that the Z factor in the DFT+DMFT calculations [4] is considerably smaller for the most correlated Ni $3d_{x^2-y^2}$ orbital. Its value was reported to be 0.36 ($LaNiO_2$, Ref. [5]). In the case of the Cu $3d_{x^2-y^2}$ orbital, the DFT+DMFT values are 0.50 ± 0.75 ($CaCuO_2$, Ref. [4]), which are not much different from ours. There are a few possible sources of the differences for $LaNiO_2$: (i) an insufficient number of diagrams included in our calculations; (ii) a single-site approximation in the DFT+DMFT calculations; and (iii) the Hubbard U was taken too large in the DFT+DMFT case. Experimental research is,

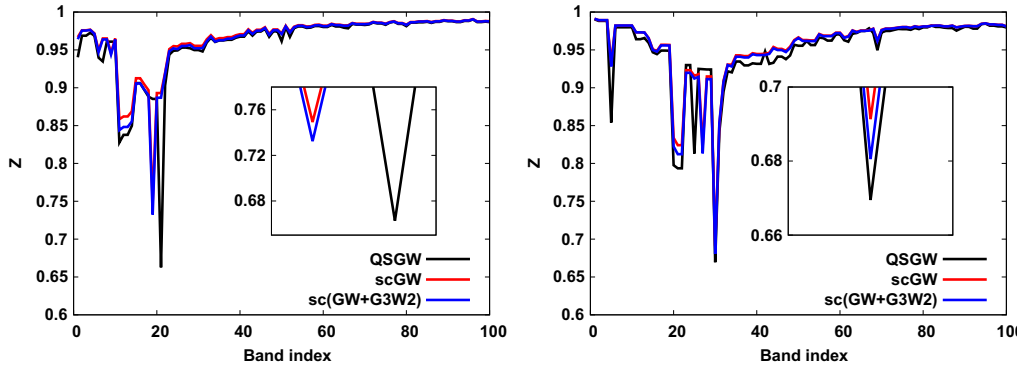

FIG. 6. Renormalization factor Z vs the band index for the Γ point in the Brillouin zone. Left window: $CaCuO_2$, right window: $LaNiO_2$. The insets magnify the area around the minimum of Z. The renormalization factor is defined as a $\mathbf{k}$-dependent matrix in the basis of band states: $Z^{-1}_{\lambda\lambda'}(\mathbf{k}) = \delta_{\lambda\lambda'} - \frac{\partial \Sigma^c_{\lambda\lambda'}(\mathbf{k};\omega)}{\partial(i\omega)}|_{\omega=0}$, with $\Sigma^c_{\lambda\lambda'}(\mathbf{k};\omega)$ being correlation self-energy. Diagonal elements of the matrix Z are plotted for $\mathbf{k} = \mathbf{0}$.

therefore, imperative for purposes of comparison. However, as all calculations neglect the electron-phonon interaction, a direct comparison with future experimental mass enhancement (for instance) will require inclusion of the electron-phonon interaction in the theoretical predictions.

A distinctive feature of the DFT+DMFT calculations is the renormalization (narrowing) of the bands near the Fermi level. For $LaNiO_2$ it is shown in Fig. 1 in Ref. [5] and for $CaCuO_2$ it is shown in Fig. 4 in Ref. [4]. The narrowing is seen particularly well along the Γ-Z direction in the Brillouin zone for the band immediately under the Fermi level ($LaNiO_2$). In the $CaCuO_2$ case, the actual bands are well entangled near the Fermi level, so that in the DMFT applications the disentanglement procedure is used. For purposes of comparison, we show in Fig. 7 the bands near the Fermi level along the path Γ-Z-R in the Brillouin zone. Figure 8 shows the DFT band structure in a larger energy window and for a larger number of $\mathbf{k}$-points. The case of $LaNiO_2$ is a bit simpler, so we discuss it first. As one can see at the Γ point, all three correlated methods [QSGW, scGW, and sc($GW + G3W2$)] result in a large narrowing of the DFT band of the Ni $3d_{x^2-y^2}$ character, which is the second band from the Fermi level at the Γ point. This band can be easily identified: it starts at -1.2 eV in the DFT case, and at about -0.5 eV in the other cases. The strongest renormalization is in the sc($GW + G3W2$) case (more than by a factor of 2), which is approximately the same renormalization as in the DFT+DMFT case [5]. The QSGW and the scGW result in only slightly smaller renormalization. The similarity with the DFT+DMFT result is interesting considering the number of differences in the methods. In the $G0W0$ calculations [10], the band narrowing along the Γ-Z path was also observed, but it was smaller by almost a factor of 2 than in our calculations because of a lack of self-consistency. If we look at the same band along the Γ-Z path, we can see the difference between the methods. The band is flat in the DFT, the DFT+DMFT, and the QSGW cases, but it has a slight but noticeable dispersion in the scGW and the sc($GW + G3W2$) cases. In the case of the DFT+DMFT, it is flat because the DMFT self-energy is independent of momenta and, correspondingly, the flatness of the DFT band remains. But the difference between the QSGW on the one hand and the scGW/sc($GW + G3W2$) on the other hand deserves attention. Taking into account the specifics of the methods, one can speculate that this difference is due to the dynamic effects (frequency dependence) in self-energy, which are included in the scGW and the sc($GW + G3W2$) methods but not in the QSGW method. Self-energy is momentum-dependent in all three methods, so the difference in its frequency dependence from one $\mathbf{k}$-point to another can result in dispersion. In the DFT, this band is crossing with another band at the Z point.

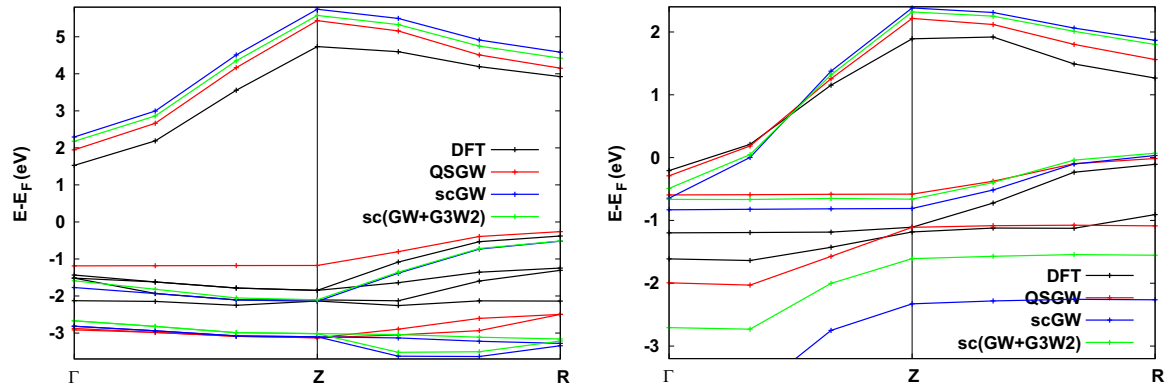

FIG. 7. Quasiparticle band structure along the Γ-Z-R path in the Brillouin zone. Left window: $CaCuO_2$, right window: $LaNiO_2$. Only the bands near the Fermi level are shown.

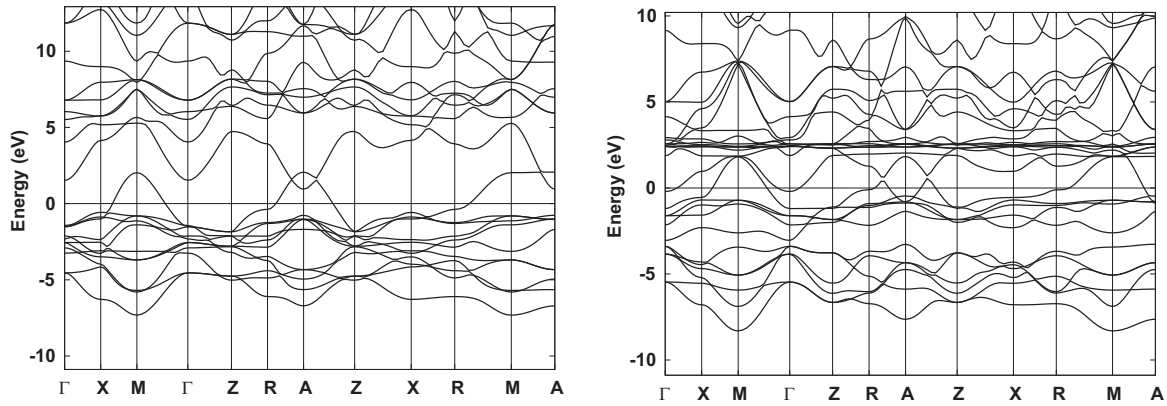

FIG. 8. DFT band structure of $CaCuO_2$ (left window) and $LaNiO_2$ (right window).

But there is no such crossing in any of the correlated methods including the DFT+DMFT. Thus, this is another similarity of our results with the DFT+DMFT results.

There is an interesting difference with the DFT+DMFT involving the size of the electron pocket near the Γ point. In the DFT+DMFT [5], its size is slightly reduced as compared to the DFT case. In our calculations, all three correlated methods show an increase of the pocket. A slight increase of the electron pocket at Γ was also reported in the $G0W0$ calculations [10]. This would be interesting to compare with experiment. However, as it represents one of the low-energy effects, the electron-phonon interaction has to be taken into account in the theoretical evaluations for a proper comparison.

In the $CaCuO_2$ case, the comparison is more complicated because of the entanglement of the bands (O $2p$ orbitals contribute significantly). The band of interest (Cu $3d_{x^2-y^2}$) is the fourth band (down from the Fermi level), and it starts at the Γ point at about −2.1 eV in the DFT case. In the correlated methods, however, this band is the first one down from the Fermi level, and it starts at about −1.5 to −1.8 eV [scGW and sc($GW + G3W2$)] and at about −1.2 eV in the QSGW case. So, the renormalization is smaller [scGW and sc($GW + G3W2$)] than in the DMFT case (Fig. 4 in Ref. [4]). Interestingly, however, in this case the narrowing is the strongest in the QSGW case, which is close enough to the DFT+DMFT result. Once again, we need experimental information in order to decide which method is the best. If the QSGW is more accurate, then we should conclude that long-range static correlation effects are more important for this material than dynamic effects. If, however, the scGW/sc($GW + G3W2$) is more accurate, the conclusion would be the opposite.

IV. CONCLUSIONS

In conclusion, we have applied three correlated methods [scGW, sc($GW + G3W2$), and QSGW] to study the electronic structure of $CaCuO_2$ and $LaNiO_2$. In the following aspects, our results are consistent with the previous DFT+DMFT studies: band narrowing near the Fermi level, orbital differentiation in the Ni(Cu) $3d$ shell, and stronger correlation effects in $LaNiO_2$ as compared to $CaCuO_2$. There are also differences with the DFT+DMFT studies. One of them consists in a quite noticeable repositioning of the spectral features away from the Fermi level in our correlated calculations. In the DMFT case, repositioning is small because only the Ni(Cu) $3d$ electrons are considered as correlated. Another notable difference consists in a lot smaller Z factor obtained in the DFT+DMFT works for $LaNiO_2$. This could be a result of the insufficient number of diagrams in our calculations, or simply the artifact of the single-site approximation and/or the too large Hubbard U parameter in the DFT+DMFT studies. Also, the change in the size of the electron pocket near the Γ point is different: a small decrease in the DMFT case and an increase in all our GW-based methods. In this respect, our GW-based approaches agree with the result found in Ref. [10] using the $G0W0$ approximation. Concerning the above-mentioned repositioning of the Ni $3d$ and O $2p$ levels below the Fermi level, we have found similarity with $G0W0$ calculations [10] in our QSGW studies, but not in our scGW or sc($GW + G3W2$) studies. We have also found that our three correlated methods differ from each other more prominently in the case of $LaNIO_2$, which is consistent with the conclusion that this material is more correlated.

The principal results of this work show that although the correlations in $LaNiO_2$ are stronger than those in $CaCuO_2$, they are still weak enough to allow applications of totally *ab initio* methods such as the scGW or the more advanced sc($GW + G3W2$) for both materials. Future photoemission experiments must explore whether there is a physics that cannot be captured by perturbative methods like scGW or sc($GW + G3W2$), thus requiring the use of nonperturbative approaches like DFT+DMFT.

ACKNOWLEDGMENTS

This work was supported by the US Department of Energy, Office of Science, Basic Energy Sciences as a part of the Computational Materials Science Program.

APPENDIX A: DETAILS OF THE EVALUATION OF SOME DIAGRAMS

In Ref. [21], the evaluation of the vertex correction to self-energy was presented as a two-step process. In the first step, the nontrivial part of the three-point vertex function Γ was evaluated. In the second step, this vertex function was combined with Green's function G and screened interaction W to form self-energy $GW\Gamma$. However, it was found later

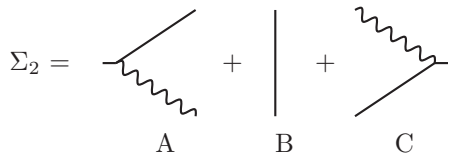

FIG. 9. Scheme of the evaluation of the second-order diagram for self-energy.

that a considerably more efficient procedure for the evaluation of second-order self-energy consists in the evaluation of the corresponding diagram directly, avoiding the intermediate construction of Γ. Namely, the second diagram presented in Fig. 3 can be evaluated in three steps, as is demonstrated in Fig. 9. The pieces A, B, and C shown in Fig. 9 are combined beginning from the right and proceeding to the left. Essentially, the algorithm is very similar to the algorithm for first-order polarizability shown schematically in Fig. 10 and described in detail in Ref. [21].

The piece C (Fig. 9) is evaluated in a (reciprocal space + frequency) representation with the band state indexes representing the orbital basis set. After evaluation, piece C is transformed into a (real space + imaginary time) representation (see Ref. [21] for the specifics of the representations of functions in real space). Thus, pieces B and C are combined in a (real space + imaginary time) representation, which can be approximately thought of as point-by-point multiplication. After that, the object B+C is transformed back to the (reciprocal space + frequency) representation, and it is combined with the piece A. In practice, this algorithm of self-energy evaluation is a few times faster than the original one presented in Ref. [21], and it requires considerably less memory.

APPENDIX B: EFFECTIVE CORRELATION SELF-ENERGY IN QS*GW*

For clarity, we define the effective correlation self-energy $\Sigma^{\rm corr}$ in QS*GW* as self-energy that transforms the Hartree-Fock Green's function $G^{\rm HF}$ into the QS*GW* Green's function $G^{\rm QP}$ via Dyson's equation:

$$\Sigma^{\rm corr} = G^{-1\rm HF} - G^{-1\rm QP}. \tag{B1}$$

In the above equation, we express all quantities in the basis of the Hartree-Fock eigen-states $\Psi_\lambda^{\mathbf{k},\rm HF}(\mathbf{r})$, where $\mathbf{k}$ is the momentum and λ stands for the Hartree-Fock band state. In this basis set, the Hartree-Fock Green's function is diagonal:

$$G^{\mathbf{k},\rm HF}_{\lambda\lambda'}(\omega) = \frac{\delta_{\lambda\lambda'}}{i\omega + \mu - \epsilon^{\mathbf{k}}_\lambda}, \tag{B2}$$

where ω is Matsubara's frequency, $\epsilon^{\mathbf{k}}_\lambda$ is the Hartree-Fock one-electron energies, and μ stands for the chemical potential. The QS*GW* Green's function in the basis of Hartree-Fock band states has the following form (see Sec. 5 in Ref. [23]):

$$G^{\mathbf{k},\rm QP}_{\lambda\lambda'}(\omega) = \sum_i \frac{Q^{\mathbf{k}}_{\lambda i} Q^{\dagger\mathbf{k}}_{i\lambda'}}{i\omega + \mu - E^{\mathbf{k}}_i}, \tag{B3}$$

with $E^{\mathbf{k}}_i$ being quasiparticle one-electron energies, and with unitary matrices $Q^{\mathbf{k}}_{\lambda i}$ representing a transformation from Hartree-Fock states to QS*GW* (QP) states, $\Psi^{\mathbf{k},\rm QP}_i(\mathbf{r}) = \sum_\lambda Q^{\mathbf{k}}_{\lambda i}\Psi^{\mathbf{k},\rm HF}_\lambda(\mathbf{r})$.

Direct substitution of (B2) and (B3) in Eq. (B1) gives a simple result:

$$\Sigma^{\mathbf{k},\rm corr}_{\lambda\lambda'} = \sum_i Q^{\mathbf{k}}_{\lambda i} E^{\mathbf{k}}_i Q^{\dagger\mathbf{k}}_{i\lambda'} - \epsilon^{\mathbf{k}}_\lambda \delta_{\lambda\lambda'}. \tag{B4}$$

As one can see, the effective correlation self-energy in QS*GW* is explicitly frequency-independent (static). However, as is also clear from the construction [23] of the QS*GW* Green's function, there is an implicit dependence of its matrix elements on the frequency. This implicit frequency dependence comes from the fact that quasiparticle energies $E^{\mathbf{k}}_i$ are obtained after the linearization of the frequency dependence of the "original" diagrammatic self-energy $\Sigma = GW$. Any change in the frequency dependence of the "original" self-energy would result in a change of the quasiparticle energies $E^{\mathbf{k}}_i$ and, as a result, a change of the effective correlation self-energy.

The absence of an explicit dependence of the QS*GW* self-energy on frequency creates certain qualitative differences between QS*GW* and self-consistent diagrammatic approaches (such as sc*GW*). For instance, there are no incoherent effects in QS*GW*, and its one-electron energies are well-defined (i.e., they have an infinite lifetime), like one-electron energies in DFT or in Hartree-Fock approximations.

APPENDIX C: FULLY SCREENED INTERACTION AS A FUNCTION OF REAL FREQUENCY

To shed a little bit more light on the differences between methods based on the well-defined quasiparticles (QS*GW*) and methods with incoherent effects [sc*GW* and sc(*GW* + *G*3*W*2)], we plot the imaginary part of the screened interaction W (Im W) as a function of real frequency (Fig. 11). The results obtained in the RPA with the LDA Green's function are also included (abbreviated as *G*0*W*0). In FLAPWMBPT code, everything is done in Matsubara's formalism. Therefore, in order to plot W as a function of real frequency, it has to be analytically continued from the imaginary to the real axis of frequencies. This was done with use of the algorithm proposed for analytical continuation (AC) of bosonic functions by Vidberg and Serene in Ref. [40]. We have to mention that for the analytical continuation of self-energy (fermionic function), we use a similar algorithm [22] which is a slight modification of the algorithm by Vidberg and Serene. There is, however, a certain difference in the degree of robustness of the AC for fermionic and bosonic functions. Whereas AC of self-energy is quite robust, which was tested on numerous materials (we do it all the time when we calculate electronic structure), the result of AC of bosonic functions is more sensitive to the quality of input information on the imaginary

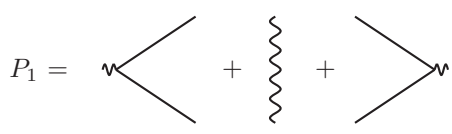

FIG. 10. Scheme of the evaluation of the first-order diagram for irreducible polarizability.

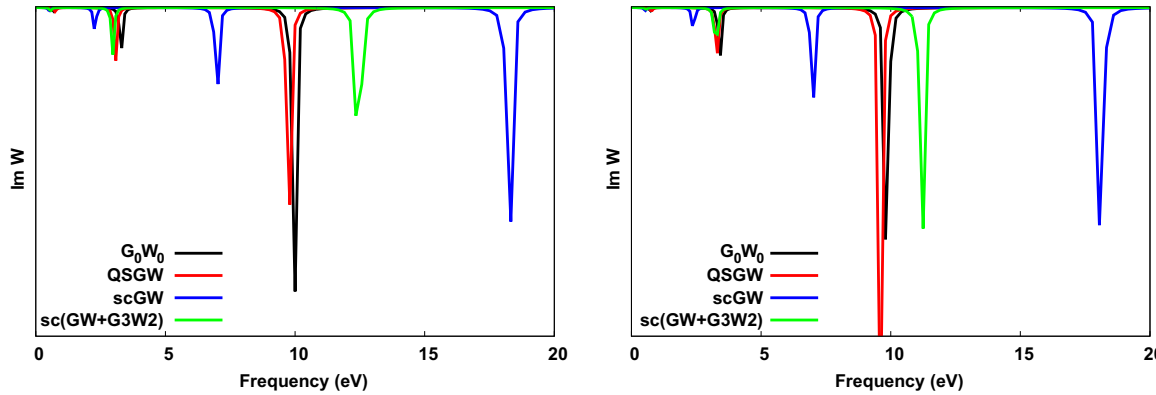

FIG. 11. Diagonal elements of the Im W evaluated for Ni $3d(yz)$ (left window) and for Ni $3d(3z^2 - r^2)$ (right window) orbitals as functions of frequency (real axis). The results are for $LaNiO_2$. As a basis set for plotting, we used solutions of the radial equations inside the muffin-tin spheres (i.e., the so called ϕ-functions of the LAPW basis set).

axis. This was noticed a few years earlier when calculating the electron energy loss spectrum (EELS) of LiF [24]. In this work, we also had to double the number of points on both imaginary time and imaginary frequency grids (from 64 to 128) in order to stabilize the positions of peaks of Im W within 0.5–1 eV. Nevertheless, the qualitative picture (relative positions of peaks obtained by different methods) did not change much during the process. With the above information kept in mind, we can see that there is a clear difference between $G0W0$, QSGW, and sc$(GW + G3W2)$ on the one hand, and scGW on the other hand. As compared to the approaches from the first group, which have only one peak in the interval 5–20 eV, scGW results in two peaks in the indicated interval of frequencies. Taking into account the fact that scGW is most likely the less accurate of the studied approaches, one can assume that the peak at about 7 eV obtained in scGW is a result of approximations. It is difficult to ascribe a precise physical meaning to the obtained peaks, partly because of the subtleties of AC and also because of the complexity of the electronic structure of $LaNiO_2$. The peaks below 5 eV are most likely the artifacts of the AC as their amplitude reduces when we increase the accuracy of the input data (W on the imaginary axis). The peaks above 5 eV are most likely of a plasmon nature, and, in this respect, the situation seems to be different from, for instance, electron gas. In electron gas [25], the plasmon poles obtained with $G0W0$ are flushed out when one uses scGW. In $LaNiO_2$, on the other hand, there are two poles in scGW instead of one pole in $G0W0$ or QSGW. When one uses the sc$(GW + G3W2)$ approximation, the number of poles in the interval 5–20 eV becomes one, and the pole is shifted toward smaller frequencies as compared to the case of scGW. In this respect, the situation is reminiscent of that in LiF [24], where the positions of the poles of the dielectric function are also shifted toward smaller frequencies when one uses a vertex-corrected scheme instead of scGW. In general, three methods [$G0W0$, QSGW, and sc$(GW + G3W2)$] seem to be consistent with each other, whereas scGW stands a bit apart.

[1] V. I. Anisimov, D. Bukhvalov, T. M. Rice, Phys. Rev. B **59**, 7901 (1999).
[2] K.-W. Lee and W. E. Pickett, Phys. Rev. B **70**, 165109 (2004).
[3] J. Kapeghian and A. S. Botana, Phys. Rev. B **102**, 205130 (2020).
[4] J. Karp, A. S. Botana, M. R. Norman, H. Park, M. Zingl, and A. Millis, Phys. Rev. X **10**, 021061 (2020).
[5] Y. Wang, C.-J. Kang, H. Miao, and G. Kotliar, Phys. Rev. B **102**, 161118(R) (2020).
[6] A. S. Botana and M. R. Norman, Phys. Rev. X **10**, 011024 (2020).
[7] P. Jiang, L. Si, Z. Liao, and Z. Zhong, Phys. Rev. B **100**, 201106(R) (2019).
[8] S. Ryee, H. Yoon, T. J. Kim, M. Y. Jeong, and M. J. Han, Phys. Rev. B **101**, 064513 (2020).
[9] Y. Gu, S. Zhu, X. Wang, J. Hu, and H. Chen, Commun. Phys. **3**, 84 (2020).
[10] V. Olevano, F. Bernardini, X. Blase, and A. Cano, Phys. Rev. B **101**, 161102(R) (2020).
[11] F. Petocchi, V. Christiansson, F. Nilsson, F. Aryasetiawan, and P. Werner, Phys. Rev. X **10**, 041047 (2020).
[12] M. Gatti, F. Bruneval, V. Olevano, and L. Reining, Phys. Rev. Lett. **99**, 266402 (2007).
[13] C. Weber, S. Acharya, B. Cunningham, M. Grüning, L. Zhang, H. Zhao, Y. Tan, Y. Zhang, C. Zhang, K. Liu, M. Van Schilfgaarde, and M. Shalaby, Phys. Rev. Research **2**, 023076 (2020).
[14] The latest publicly available version of the FLAPWMBPT code can be downloaded from the website https://github.com/andreykutepov65/FlapwMBPT. Calculations in this work were performed with an updated version that can be requested from the author using e-mail: akutepov@bnl.gov. Input files that can be used for reproducing the results of this work can also be requested from the author.
[15] J. P. Perdew and Y. Wang, Phys. Rev. B **45**, 13244 (1992).
[16] A. L. Kutepov, Phys. Rev. B **103**, 165101 (2021).
[17] A. L. Kutepov, J. Phys.: Condens. Matter **33**, 235503 (2021).
[18] L. Hedin, Phys. Rev. **139**, A796 (1965).

[19] C.-O. Almbladh, U. von Barth, and R. van Leeuwen, Int. J. Mod. Phys. B **13**, 535 (1999).
[20] J. M. Luttinger and J. C. Ward, Phys. Rev. **118**, 1417 (1960).
[21] A. L. Kutepov, Phys. Rev. B **94**, 155101 (2016).
[22] A. Kutepov, K. Haule, S. Y. Savrasov, and G. Kotliar, Phys. Rev. B **85**, 155129 (2012).
[23] A. L. Kutepov, V. S. Oudovenko, and G. Kotliar, Comput. Phys. Commun. **219**, 407 (2017).
[24] A. L. Kutepov, Phys. Rev. B **95**, 195120 (2017).
[25] B. Holm and U. von Barth, Phys. Rev. B **57**, 2108 (1998).
[26] A. Kutepov, S. Y. Savrasov, and G. Kotliar, Phys. Rev. B **80**, 041103(R) (2009).
[27] A. L. Kutepov, J. Phys.: Condens. Matter **29**, 465503 (2017).
[28] W.-D. Schöne and A. G. Eguiluz, Phys. Rev. Lett. **81**, 1662 (1998).
[29] M. Grumet, P. Liu, M. Kaltak, J. Klimes, and G. Kresse, Phys. Rev. B **98**, 155143 (2018).
[30] A. L. Kutepov, arXiv:2106.03800.
[31] L. Boehnke, F. Nilsson, F. Aryasetiawan, and P. Werner, Phys. Rev. B **94**, 201106(R) (2016).
[32] A. Stan, N. E. Dahlen, and R. van Leeuwen, Europhys. Lett. **76**, 298 (2006).
[33] A. Stan, N. E. Dahlen, and R. van Leeuwen, J. Chem. Phys. **130**, 114105 (2009).
[34] F. Caruso, P. Rinke, X. Ren, M. Scheffler, and A. Rubio, Phys. Rev. B **86**, 081102(R) (2012).
[35] A. L. Kutepov and G. Kotliar, Phys. Rev. B **96**, 035108 (2017).
[36] A. L. Kutepov, arXiv:2105.07798.
[37] T. Kotani, M. van Schilfgaarde, and S. V. Faleev, Phys. Rev. B **76**, 165106 (2007).
[38] M. Shishkin, M. Marsman, and G. Kresse, Phys. Rev. Lett. **99**, 246403 (2007).
[39] J. R. Naegele, L. Manes, J. C. Spirlet, and W. Müller, Phys. Rev. Lett. **52**, 1834 (1984).
[40] H. J. Vidberg and J. W. Serene, J. Low Temp. Phys. **29**, 179 (1977).
[41] A. L. Kutepov, Comput. Phys. Commun. **257**, 107502 (2020).